Seasonal to interannual variability of the tide in the Amazon estuary

Alice César Fassoni-Andrade, Fabien Durand, Alberto Azevedo, Xavier Bertin, Leandro Guedes Santos, Jamal Uddin Khan, Laurent Testut, Daniel Medeiros Moreira

Seasonal to interannual variability of the tide in the Amazon estuary

Alice César Fassoni-Andrade[1,2], Fabien Durand[1,2], Alberto Azevedo[3], Xavier Bertin[4], Leandro Guedes Santos[5], Jamal Uddin Khan[4], Laurent Testut[4], Daniel Medeiros Moreira[6,7]

[1]Laboratoire d'Etudes en Géophysique et Océanographie Spatiales (LEGOS), Université Toulouse, IRD, CNRS, CNES,UPS, Toulouse, France

[2]University of Brasília (UnB), Institute of Geosciences, Brasília, Brazil

[3]Laboratório Nacional de Engenharia Civil (LNEC), Avenida do Brasil 101, Lisboa, Portugal.

[4]LIENSs UMR 7266, CNRS- La Rochelle University, 17000 La Rochelle, France

[5]CPRM, Serviço Geológico do Brasil, Avenida Doutor Freitas, 3645, Marco, Belém, Brazil.

[6]CPRM, Serviço Geológico do Brasil, Avenida Pasteur, 404, Urca, Rio de Janeiro, Brazil.

[7]GET, CNRS/CNES/IRD/UPS, 31400 Toulouse, France

Abstract

The Amazon River exports the largest volume of fresh water to the ocean worldwide.. Although previous studies have revealed the spatiotemporal tidal variability of the estuary, its hydrodynamics is still poorly understood. Here we evaluate the seasonal and interannual variability of the tide from Óbidos (800 km upstream) to the Atlantic Ocean and show how it is affected by the hydrological regime of the Amazon River. A high-resolution 2D hydrodynamic model was applied in this region at the scale of the whole estuary. The tide model is validated using data from 14 water level stations and shows an average complex error of 16 cm in the low flow season and 23 cm in the high flow season. The semi-diurnal tide is highly variable at seasonal timescales, and the seasonality of the discharge affects the tidal amplitude, the geographic extent of tidal influence, the tidal wave celerity, and the tidal flow reversal. Notably, the tidal influence on water level remains detectable up to Óbidos during the low flow season while during the high flow season it extends from the ocean to only 300 km downstream of Óbidos. On the other hand, the upstream limit of the domain where the tide induces a periodic flow reversal is different from the limit of tidal influence on the water level. The upstream limit of this flow reversal is shifted by 170 km (from 500 km to 670 km downstream of Óbidos) along the year due to the seasonality of the discharge. At interannual scale, anomalous hydrological discharges affect the tidal amplitude by up to 30% in the central reach of the estuary. Our findings open

unprecedented opportunities to understand biogeochemical and geomorphological processes, help navigation, and assess flooding hazards.

Highlights

Advances in modeling the impact of Amazon River variability on tidal modulation

Tidal amplitude and phase are well represented with a complex error of order 20 cm

River discharge controls tidal range, tidal celerity, and flow reversal

Extreme discharges induce changes of 10-25% of the tidal range in the central estuary

1. Introduction

The Amazon is the largest continental freshwater supply to the world ocean, with an average discharge of 200 thousand m^3/s (Callède et al., 2010). It drains a watershed of more than 6 million km^2, encompassing about one-third of South America. The lower part of the watershed consists of a very long estuary extending over 800 km downstream of Óbidos meeting the Atlantic Ocean (Figure 1; Kosuth et al., 2009). On one hand, the tide propagates up to Óbidos due to the weak slope of the riverbed. On the other hand, the consistently high discharge throughout the seasonal cycle prevents salty ocean waters from entering the estuary (Geyer and Kineke, 1995), unlike most estuaries. The knowledge of temporal (seasonal to inter-annual) variability of tide with freshwater inflow is required to better understand the sediment transport and morphodynamics of the estuary and adjacent floodplains (Fricke et al., 2019; Nittrouer et al., 2021), as well as the ecology and biogeochemical balance of the river and floodplains (Junk et al., 2012; Melack et al., 2021; Sawakuchi et al., 2017).

The Amazon River flood period (high flow) occurs in May/June and the drought period (low flow) in October/November (Figure 1d). This annual variation in water level results in the periodic inundation of the large and shallow floodplains in the upper reach of the estuary (~250 km in extent; Fricke et al., 2019). The tidal influence in this reach is observed only during the low flow period and is smaller than in the downstream part of the estuary (Kosuth et al., 2009). However, the adjacent floodplains may exert some, yet unknown, effect on tidal variability (Fortunato and

Oliveira, 2005). The middle reach of the estuary (Almeirim region, Figure 1) has few floodplains more connected to the river due to absence of levees (Fricke et al., 2019) and a straight river channel. Downstream of this point, the river splits into two large channels and ends in a deltaic network of tributaries, where the tide has the most significant influence on the water level.

The mouths of the Amazon outflow over a broad, shallow shelf and are characterized by a macrotidal regime. The tidal amplitude reaches 2 m in the Amazon mouth, with values over 3 m locally on the northern side of the Amazon mouth, making it one of the most energetic tidal regions of the tropical Atlantic basin (Ruault et al., 2020). The large tidal amplitude at the Amazon mouths results from the combination of two effects. The first one is the ideal geometry of the Amazon shelf regarding the resonance of the semi-diurnal tidal waves incoming from the deep ocean (Beardsley et al., 1995; Clarke and Battisti, 1981). The second is the consistent presence of extended fluid mud layers deposited by the Amazon plume, limiting tidal dissipation on the bottom over the shelf (Gabioux et al., 2005; Kineke et al., 1996; Le Bars et al., 2010).

The observational study of Kosuth et al. (2009) described the characteristics of the tide propagating in the Amazon estuary, based on an original set of in situ gauge records collected along the various reaches in the late 1990s. They documented the seasonal variability of the tidal range and the phase speed of the tidal waves, showing a contrasting situation between the high and the low flow periods. During the high flow season, the tidal amplitude is typically twice as weak as during the low flow season, all over the central part of the Amazon estuary, some 400 km downstream of Óbidos.

The modelling of the tidal dynamics of the Amazon estuary and adjoining shelf remains a challenging research topic. Whereas there exist several numerical modeling studies that investigated the tidal hydrodynamics of the Amazonian shelf (Durand et al., 2022; Fontes et al., 2008; Gabioux et al., 2005; Molinas et al., 2020, 2014; Nikiema et al., 2007; Ruault et al., 2020), the past studies dedicated to the hydrodynamic modeling of the inner Amazon estuary are scarce. However, they provided valuable insights on the mechanisms of tidal propagation and its interaction with the Amazon discharge. The pioneering modelling study of Gallo and Vinzon (2005) shed light on the non-linearity of the tidal dynamics in the lower Amazon,

yielding strong shallow-water tidal constituents that give rise to a marked asymmetry of the semi-diurnal tide, as well as to a strong signature of the fortnightly tide. Furthermore, they provided evidenced for the key role of bottom friction in generating both M4 and MSf constituents all along the estuary. The gradual increase of MSf fortnightly constituent combined with the gradual decay of primary semi-diurnal constituents M2 and S2 from the mouths towards upstream was found to induce a peculiar behavior of the Amazon spring-neap cycle. Over the central reach of the estuary, low waters at spring tide were found to be sitting at levels typically 0.2 m higher than the low waters at neap tide. Despite these already documented complex hydrodynamic features, to date, a seamless hydrodynamic modeling framework encompassing the whole Amazon estuary at high resolution and resolving the seasonal to interannual timescales of variability of the tide is still lacking.

There have been numerous studies investigating the relationship between river discharge and tidal characteristics in other large estuaries (e.g., Cai et al., 2014; Elahi et al., 2020; Godin, 1999; Guo et al., 2015; Helaire et al., 2019; Jay et al., 2011; Losada et al., 2017; Matte et al., 2014). To the best of our knowledge, however, the present study is the first to model the hydrodynamics over the Amazon estuary with a high-resolution numerical model, explicitly accounting for the seasonal-to-interannual variability of the hydrological regime of the river discharge. It relies on a seamless unstructured-grid numerical model extending from Óbidos down to the deep Atlantic Ocean. Our objective is to document the characteristics of the tide all along the Amazon estuary and across its timescales of variability from the high-low flow seasonal cycle to the interannual anomalous hydrological events.

Section 2 presents the numerical modeling framework and the datasets we use for the model validation. Section 3 is dedicated to the validation of the model. In section 4, we present the seasonally-varying tidal characteristics of the Amazon estuary. Section 5 investigates the case of the anomalous years, contrasting positive and negative discharge extremes. A brief conclusion ends the paper (Section 6).

2. Data and methods

The study relies on a hydrodynamical modeling platform implemented over the whole Amazon Estuary down to the adjoining Atlantic Ocean shelf and beyond, until the Atlantic abyssal plain. For developing the model, we have used a state-of-the-art

bathymetric atlas of the region (Fassoni-Andrade et al., 2021). We hereafter detail the salient features of the modeling tool, the bathymetric atlas, and the independent datasets we used for model validation.

2.1 Model

The SCHISM (Semi-implicit Cross-scale Hydroscience Integrated System) model (Zhang et al., 2016) was used to simulate the tides and river flow of the Amazon River along the estuary. SCHISM solves the 3D shallow-water equations using finite-element and finite-volume schemes. It was designed to model barotropic and baroclinic flows over a broad range of spatial scales, spanning from the deep parts of the open ocean to very shallow estuaries and lagoons (e.g., Huang et al., 2021; Khan, 2021; Khan et al., 2020). It comprises a wetting/drying scheme for the shallow zones. The model was used in depth-averaged 2DH mode, similar to previous studies of comparable tropical mega-delta regions conducted with this model (e.g., Khan et al., 2020; Krien et al., 2016).

The model domain covers the 435 thousand km^2 from Óbidos to the ocean, encompassing floodplains and intertidal zones. The ocean open boundary is limited to tracks 024 and 215 of the Jason series satellite altimetry missions (Figure 1a). Spaceborne altimetry allows to accurately estimate tidal constituents available through the AVISO products (www.aviso.altimetry.fr/en/data/products/auxiliary-products/coastal-tide-xtrack.html). Aligning the model open boundaries along altimetric tracks enables the imposition of the accurate tidal boundary conditions observed there, following the strategy of Testut and Unnikrishnan (2016). The altimetric tidal constituents along these tracks are indeed more accurate than in state-of-the-art tidal atlases (Le Bars et al., 2010). Besides, a large domain extending far from the Amazon mouths ensures that the shallow-water non-linear tidal constituents can develop and propagate freely within the model interior domain (Gallo and Vinzon, 2005). The tidal constituents considered at the boundary conditions were M2, M3, M4, M6, Mf, Mm, MN4, MS4, MU2, N2, NU2, O1, P1, Q1, R2, S1, S2, S4, SA, SSA, T2, Msf, K2, K1, J1, and 2N2. Inside the model domain, the tidal potential of M2, S2, T2, Q1, P1, O1, NU2, N2, MU2, L2, K2, and K1 constituents is imposed.

A pre-defined flood mask limits the model domain over the continent, as follows. The maximum water level was estimated following the methodology defined

in the study by Fassoni-Andrade et al. (2021). First, over the inner river, it was estimated considering data from 2015 to 2018 at gauge stations. Then, over the coastal region, it was estimated based on a proxy of the syzygy tidal amplitude defined from the sum of M2 and S2 constituent amplitudes from the FES2014 tidal atlas (Carrère et al., 2016). This estimated maximum water level was then increased by 2 m for safety and interpolated by the nearest-neighbor method over the domain of a Digital Elevation Model (DEM; described in the next section). Subsequently, considering this maximum water level, the floodable/non-floodable pixels over the whole DEM were identified to create a flood mask. Therefore, the model domain consists of the area located up to 2 m above the maximum water level observed during the 2015-2018 period (in the inner estuary) and up to 2 m above the maximal tidal level (along the ocean shoreline).

The model was implemented on an unstructured mesh considering triangular cells with a varying spatial resolution using SMS (Surface-water Modeling System) software (© Aquaveo; Figure 1b). The elements' size was defined by a combination of two geographic criteria, one based on the value of the local bathymetry and another based on the strength of the bathymetry gradient, in a fashion similar to Krien et al. (2016). This meshing strategy ensures a faithful representation of the propagation of gravity waves both in shallow waters and in regions with higher bottom slope. The minimum mesh elements size reaches 250 m, all along the bed of the estuary. It amounts to about 400 m in the upstream floodplain region (Area 1 in Figure 1a) and gradually increases offshore of the estuary mouths, up to 5000 m in the deeper parts of the ocean (Area 2 in Figure 1a). In addition, the orientation of the mesh cell faces on the riverbanks was imposed along the levees to better represent the flow exchange between the river and the adjacent floodplains. Altogether, this unstructured meshing strategy allows to represent the inundation satisfactorily in the shallow areas of the upper floodplains (depth ~1m in low flow period) and also allows to avoid unnecessary, costly mesh cells in the deep ocean. The mesh has 688'636 nodes and 1'362'336 elements in total.

Friction was represented by a Manning's roughness coefficient based on the classification of Bunya et al. (2010), according to the classes displayed on the map in Figure 1c. Vegetation was classified according to height (greater and less than 1 m) according to Global Forest Canopy Height (GEDI, Potapov et al., 2021), which

represents the height of vegetation globally at 30 m resolution (Landsat; available at www.glad.umd.edu/dataset/gedi). The water class on this map was classified into river, floodplain, and ocean. The fluid mud extent off the mouths was considered according to Gabioux et al. (2005). The Amazon River exports a large amount of sediments to the ocean (1.1×10^9 tons per year; Armijos et al., 2020), and fluid mud gets deposited in the shallow region situated in the vicinity of the mouths. It contributes to reduced energy dissipation of the tide. Gabioux et al. (2005) showed that not representing the mud in a hydrodynamic model of the region can drastically underestimate the amplitude of M2 tide. By conducting a set of sensitivity experiments of our model with or without this region of low friction (red area in Figure 1c), as well as with or without the transition zone upstream of it (orange area in Figure 1c), we could confirm that the realism of the modeled tide improves significantly when both these features are present in our modeling setup (not shown).

Discharges of the Amazon, Tapajós, Xingu, and Pará rivers were used as boundary conditions in the model considering the year 2018 (Figure 1d). That year can be considered as a roughly normal year in terms of runoff for the Amazon, which is by far the main contributor to the freshwater delivered to the Atlantic Ocean. The Amazon River discharge at Óbidos varies from 100'700 $m^3.s^{-1}$ to 225'210 $m^3.s^{-1}$ between November and May, with average annual values of 168'480 $m^3.s^{-1}$ (climatology between 1968 and 2020). Based on sparse in situ observations, it was reported that about 1% of the Amazon River discharge flows through the Breves Channel into the Pará River estuary (Callède et al., 2010). Therefore, the value of 1% of the Amazon runoff imposed in our model was considered an outflowing boundary condition through the Breves Channel (see location in Figure 1c). The discharges of the Tapajós (Itaituba Station), Xingu (Belo Monte Station) and Pará (Tucurui Station) rivers were obtained by the Operador Nacional do Sistema Elétrico National (www.ons.org.br/Paginas/resultados-da-operacao/historico-da-operacao/dados_hidrologicos_vazoes.aspx), and the Amazon River discharge from Agência Nacional de Águas (ANA; Óbidos Station; www.snirh.gov.br/hidroweb/serieshistoricas).

Thanks to its semi-implicit time-stepping combined with an Eulerian-Lagrangian method to treat the momentum advection, the model allows for using large time steps corresponding to CFL conditions well above unity, despite the

relatively high spatial resolution of the mesh (Zhang et al., 2016). We used in this study a 10 min timestep. We integrated the model from November 2013 to January 2019, starting from rest. We discarded the first 3 months to allow for the initial spinup.

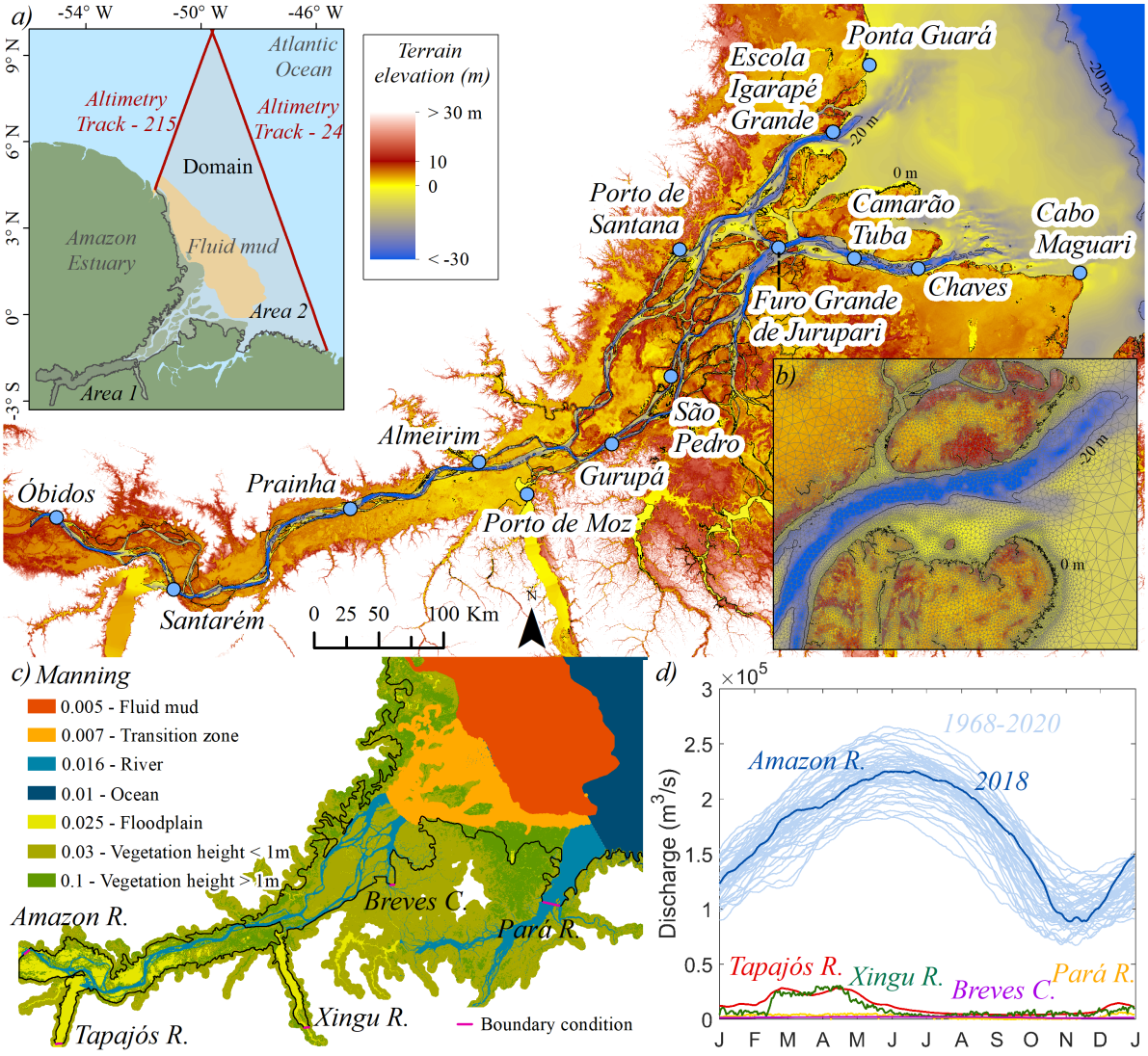

Figure 1. Bathymetry and topography of the study area and in situ stations with (a) the location of the model domain (black outline + altimetry tracks); (b) inset of the model mesh at the mouth of the Amazon; (c) Manning coefficient map; (d) Rivers discharges considered in the boundary conditions.

2.2 Data and processing

We implemented the model on the bathymetric atlas of the region, described in Fassoni-Andrade et al. (2021; available in https://data.mendeley.com/datasets/3g6b5ynrdb/2), that represents the topography

of river, floodplain, riverbanks, and ocean at 30 m resolution with accuracy of 7.2 m (riverbed) and 1.2 m (non-vegetated intertidal floodplains). The information is derived from a synthesis of global databases such as MERIT DEM (http://hydro.iis.u-tokyo.ac.jp/~yamadai/MERIT_DEM/; Yamazaki et al., 2017), GEBCO (https://www.gebco.net/) and local estimates of the river and floodplains depth.

Fassoni-Andrade et al. (2021) reported a bias of the elevation in seasonally-flooded areas of the bathymetric atlas (e.g., floodplains and river banks), which magnitude increases with decreasing flood frequency, i.e., higher areas have a larger error. To simply correct this bias, a linear fit between the bias and the flood frequency (FF) was considered in the areas with flood frequency between 0 and 78.85% following the equation:

$$bias = -0.03769 * FF + 2.972 \quad (1)$$

The biases observed along 6 in situ cross-sections of the Amazon River, with values ranging from 0.58 m to 11.68 m (Fassoni-Andrade et al., 2021), were also accounted for to correct the river bathymetry, which was achieved through linear interpolation of the observed biases between each pair of cross-sections. The resulting bathymetry and topography are shown in Figure 1.

In such a geographical context, where complex geometry implies strong spatial variability of the tides, special care must be devoted to validating the modeled tide. This validation was based on a set of in situ water level records of several stations that we could access along the estuary course. The gauge records originate from Agência Nacional das Águas of Brazil, from the Brazilian Navy, from the brazilian Instituto Brasileiro de Geografia e Estatística (IBGE) and from the french Institut de Recherche pour le Développement (IRD; Alain Laraque, personal communication). The water level records were vertically referenced to EGM08 geoid height, based on the leveling procedure explained in Fassoni-Andrade et al. (2021). Additionally, we collected a tidal record from the São Pedro station in a field campaign. In total, 14 gauging stations could be considered. Table 1 shows the characteristics of these water level records used in validation (locations are displayed in Figure 1), the list of the main tidal constituents considered in the harmonic analysis, and the period we could analyze, contrasting low and high flow seasons. The harmonic analysis was performed using the COMODO-toolbox (Allain, 2016), equally

for the modeled and observed water level records considering a 32-day window, which allows analyzing the constituents M2, S2, M4, Mm, and MSf, known as the dominant ones over our area (Gallo and Vinzon, 2005). For some stations, however, the observational record was shorter, which did not allow to analyze MSf, nor to document the low vs high flow seasons (these stations are mostly located in the downstream-most region of the estuary, see Table 1).

The error of the model tide was computed as the modulus of the complex difference for the constituents M2, S2, Mm, and M4 for each station, following the method used in Krien et al. (2016):

$$|\Delta z| = \left|A_m e^{i\theta_m} - A_o e^{i\theta_o}\right|$$

where A and θ are the amplitude and phase, respectively, of the tidal harmonic for the model (m) and the observation (o). Following Andersen et al. (1995), the total complex error at a given station is:

$$\sigma = \sqrt{\frac{1}{2}\sum_{M2,S2,M4,Mm} |\Delta z|^2}$$

Table 1. List of tide gauge records available. The relative distance is expressed in km downstream from Óbidos (for the stations located along the main course of the Amazon and the northern channel of the delta) or from Porto-de-Moz (for the stations located along the southern channel of the delta).

Station	Position	Data source	Relative distance (km)	Location	Constituents	Period analyzed	
						Low flow	High flow
Óbidos	55.51816°W 1.91866°S	ANA	0.00	Amazon R.	M2, S2, M4, Mm, Msf	Oct 2018	May 2018
Santarém	54.725°W 2.41667°S	ANA	115.83	Amazon R.	M2, S2, M4, Mm, Msf	Oct 2018	May 2018
Prainha	50.48055°W 1.80917°S	IRD	284.91	Amazon R.	M2, S2, M4, Mm, Msf	Sep 2000	May 2000
Almeirim	52.5769°W	ANA	397.08	Amazon R.	M2, S2, M4,	Oct	Junho

	1.53317°S				Mm, Msf	2018	2018
Porto de Santana	51.16774°W 0.06135°S	IBGE	672.34	North C.	M2, S2, M4, Mm, Msf	Oct 2017	May 2017
Escola Igarapé Grande	50.11536°W 0.761667°N	Brazilian Navy	827.11	North C.	M2, S2, M4, Mm, Msf	Oct 2018	May 2018
Ponta Guará	49.883333° W 1.216667°N	Brazilian Navy	892.11	Coast	M2, S2, M4, Mm	April 1970	
Porto de Moz	51.241175° W 1.753283°S	IRD	0.00	South C.	M2, S2, M4, Mm, Msf	Nov 2000	May 2000
Gurupá	51.65090°W 1.40794°S	IRD	73.56	South C.	M2, S2, M4, Mm, Msf	Sep 2000	May 2000
São Pedro	0°56'24"S, 51°14'57"W	This study	157.63	South C.	M2, S2, M4, Mm	May 2020	
Furo Grande de Jurupari	50.58500°W 0.02666°S	Brazilian Navy	291.90	South C.	M2, S2, M4, Mm	April 2008	
Camarão Tuba	49.51987°W 0.23006°S	Brazilian Navy	355.14	South C.	M2, S2, M4, Mm	April 2008	
Chaves	49.98383°W 0.16640°S	Brazilian Navy	405.06	South C.	M2, S2, M4, Mm	July 1966	
Cabo Maguari	48.41662°W, 0.25298°S	Brazilian Navy	535.06	Coast	M2, S2, M4, Mm	April 2008	

3. Model validation and limitations

Over such a long and flat estuary (< 1.5 cm/km; Birkett et al., 2002) the tidal propagation results from a delicate balance between various factors, in particular the geometry of the river bed, its elevation profile with respect to the geoid, the spatial structure of the bottom roughness, and the intensity of the residual river flow (eg., Gabioux et al., 2005; Gallo and Vinzon, 2005; Le Bars et al., 2010). To make sure that we do not have prominent error compensations among these various factors in the modeled tide, we present the following two-steps validation strategy: we first validate the tidal amplitudes and phases along the estuary, then we validate the mean (in a sense: tide-free) water slope. For the observations, the mean water level is referenced to the EGM08 geoid model (Fassoni-Andrade et al., 2021). The model-data tidal comparison is made separately during the low flow and the high flow

311 seasons, as the tidal dynamics of the estuary are known to be markedly different in
312 these two seasons (Gallo and Vinzon, 2005; Kosuth et al., 2009).

313 In line with the previous studies (e.g., Durand et al., 2022; Gallo and Vinzon,
314 2005; Ruault et al., 2020), we observed that M2 is the dominant tidal constituent at
315 the mouths of the Amazon. Figure 2 shows the complex error of the modeled tide
316 (considering M2, S2, M4, and Mm) at the stations for the low flow period (October)
317 and high flow period (May) as well as the observed and simulated M2 amplitude and
318 phase in these two periods. In addition, for the stations located downstream of
319 750km from Óbidos (stations 6, 7, 11, 12, 13, 14), the FES2014 atlas (Carrère et al.,
320 2016) is also presented (as these stations lie within FES2014 domain). Amplitudes
321 and phases of the remaining dominant constituents (S2, M4, MSf, and Mm) can be
322 seen in Table A.1 and Table A.2 (Appendix), as well as the values of the
323 corresponding complex error Table A.3 (Appendix).

324 Overall, the model represents the amplitude and phase of the main tidal
325 constituents well, with an average complex error of 16 cm in low flow and 23 cm in
326 high flow period. The complex error is lower for most stations in the high flow period
327 (May), when the Amazon River discharge is higher than in the low flow period
328 (October), especially at the Prainha station. Note that the observational record at this
329 station was of September 2000 (Table 1) when the Amazon River discharge was
330 higher than in October 2018 (period of the model simulation). The model's realism
331 appears roughly comparable with that of the global FES2014 atlas, both for
332 amplitude and phase of M2, over the downstream-most part of the estuary (Figure 2).

333

334

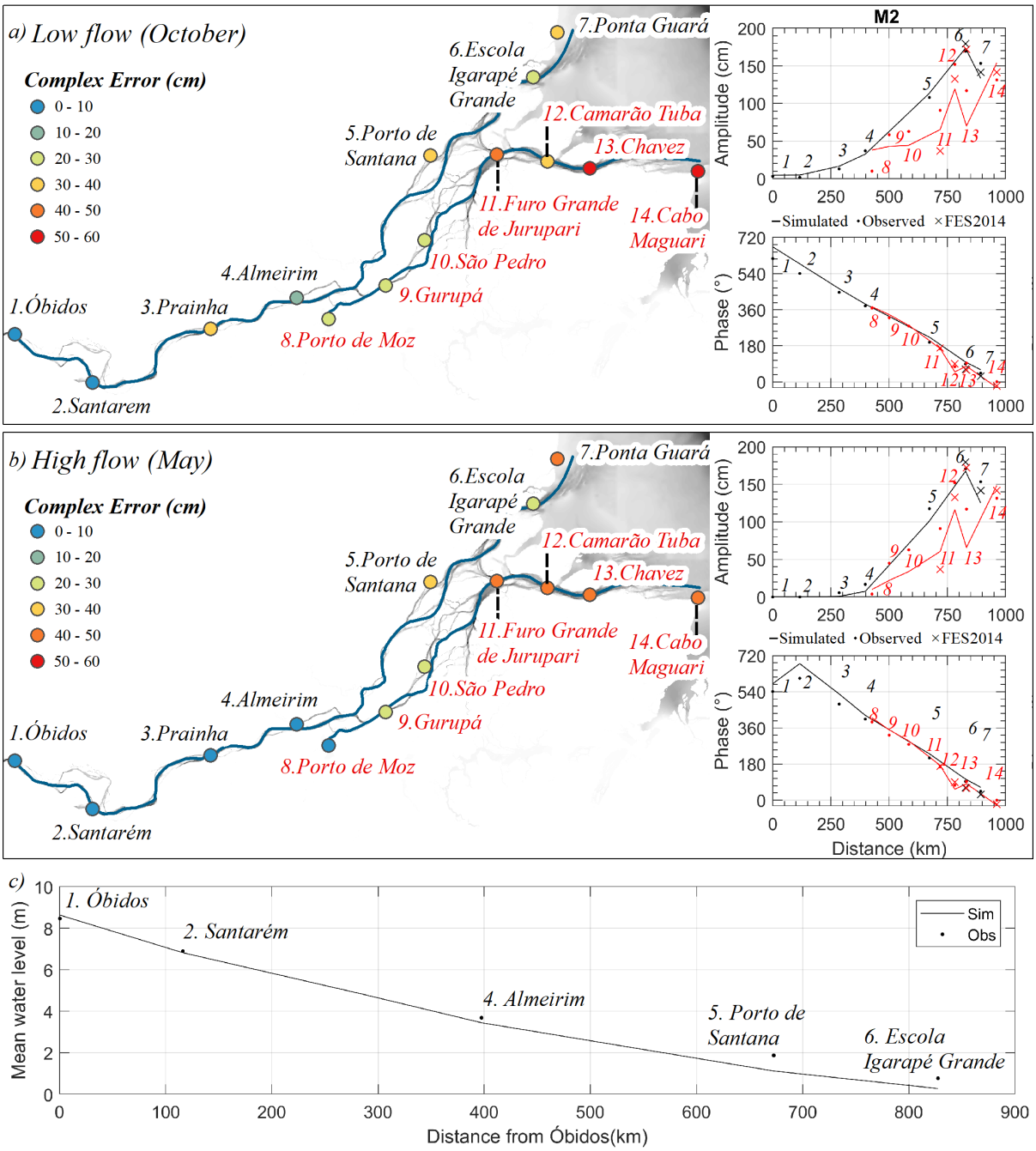

Figure 2. The total complex error along the path of the rivers for the 14 stations is shown on the map with associated color scale. On the right panel M2 amplitude and phase observed and simulated during a) low flow season (October) and b) high flow season (May). Black lines and black symbols represent the reach between Óbidos and Escola Igarapé Grande (through the Northern Channel downstream of Almeirim); red lines and red symbols represent the reach between Porto de Moz and Cabo Maguari, through the Southern Channel. The solid lines represent the model, the dots represent the observed values, and the crosses represent the FES2014 tidal atlas (which covers only the delta's downstream-most part). c) Mean annual water

345 level relative to geoid along the river, for the model (solid) and the observations (dots;
346 referenced to EGM08 geoid model).

347 The tidal amplitude for the M2 constituent at the mouth is 2 m. Due to the
348 weak slope of the terrain all along the estuary, during the low-flow period, the tide
349 propagates over 800 km upstream, up to Óbidos (and even slightly beyond in our
350 model), with typical observed tidal amplitudes of M2 amounting to about 3 cm there.
351 Overall, the phase of M2 along the estuary spans practically two cycles so that the
352 tide takes a bit less than one day to reach Óbidos. In other words, at any given time,
353 the Amazon estuary holds two successive semi-diurnal tidal waves, from its mouth to
354 Óbidos (note that the y-axis for the phase of M2 on Figure 2 goes up to 720°).

355 The M2 amplitude in the Northern Channel (black lines and dots in Figure 2)
356 appears better represented than in the Southern Channel (red lines and dots in
357 Figure 2), where larger underestimations are seen. Consistently with what was
358 known from past observational records, the observed M2 amplitude gets divided by a
359 factor of two after traveling around 500-600 km within the estuary in the low flow
360 season; during the high flow season, it gets a similar attenuation after traveling
361 around 350-400 km. Locally, we observe biases in M2 amplitude that can get as
362 strong as 50 cm at some of the coastal gauging stations where the records are
363 ancient (typically 50 years old or so; see, for instance, Chaves and Ponta Guará
364 records) and, as such, could have been affected by long-term changes of the tidal
365 characteristics resulting from morphological changes over the intervening period.
366 However, for the present study focused on the inner Amazon estuary, the bias in the
367 modeled M2 amplitude at the entrance of the estuarine system in Porto de Santana
368 is relatively weaker (17 cm or 17% in high flow season, 7 cm or 6% in low flow
369 season). Further upstream, the error in M2 amplitude further decays, along with the
370 decay of the tidal amplitude itself, in both seasons.

371 The phase of the M2 wave also appears satisfactorily represented by the
372 model. Both the observations and the model feature a roughly linear phase increase
373 from the mouth towards upstream, indicating a roughly constant phase speed of the
374 tidal wave in the propagation course. However, the modeled phase of M2 appears a
375 bit overestimated by the model, i.e., the phase speed of the tide is slightly too slow
376 along the river. At Porto de Santana, the error is 22° in the high flow period (45
377 minutes) and 28° in the low flow period (57 minutes). At Óbidos, the delay is 40°

(1h20min) and 45° (1h30min) during the high and low flow seasons, respectively. For reference, Gallo and Vinzon (2005) also found low errors of the M2 amplitude (even lower than ours, typically of 5-10 cm), but no information was provided about the tidal phase nor its error. On the other hand, Le Bars et al. (2010) found phase errors ranging from 60° (about 2 h) to 150º (about 5 h) in the downstream and central parts of the estuary.

The simulated and observed mean water level profiles along the river computed throughout 2018 are presented in Figure 2c. In Óbidos, the mean water level amounts to slightly more than 8 m above the geoid. The observed mean water level shows a slope of about 1 cm/km, slightly decreasing downstream, which is satisfactorily captured by the model. The typical model error amounts to 15 cm from Óbidos to Almeirim, and 50 cm at the mouth of the northern channel (Escola do Igarapé Grande – station 6), where the mean water level gets close to geoid height. We observe the most substantial bias of the model mean water level in Porto de Santana (station 5), where it amounts to 75 cm.

There are several limitations in our modeling framework. First, we remind that our model is two-dimensional. This implies that the parameterization of the bottom friction in regions of extremely fine sediments such as the fluid mud layers reported in the near-shore ocean off the mouths of the terminal delta may be better represented in a three-dimensional modeling framework representing the dynamics of fine sediments (Molinas et al., 2020). Although unprecedented at the scale of this mega-estuary, the horizontal resolution of our model mesh may also benefit from further refinement, particularly in the very shallow seasonally-flooded floodplains located on both sides, along the main course of the estuary. Obviously, although the greatest care was devoted to the assembly of our bathymetric atlas, it is also subject to biases, in this highly dynamic and coarsely monitored sedimentary environment (Fassoni-Andrade et al., 2021). Finally, the accuracy and consistency of the rivers discharge estimates available for our model upstream boundary conditions are also subject to debate.

This said, thanks to a novel comprehensive bathymetry-topography dataset, and to an unstructured-grid high-resolution modeling system, we obtained an overall acceptable simulation of the mean water line as well as of the tide across the Amazon estuary. The typical error of our modeling appears in line with the

411 performances obtained in other poorly-observed, tropical mega-deltas, where the
412 issue of poorly known bathymetry is common (see, e.g., Elahi et al., 2020; Eslami et
413 al., 2019; Khan et al., 2020). The level of consistency achieved by our model with
414 regards to the in situ records allows us to investigate confidently the temporal
415 variability of the tidal characteristics all along the course of the estuary, over a broad
416 range of temporal scales from seasonal to interannual.

417

418 ## 4. Seasonal variability of the tide along the Amazon estuary

419 As we saw in the introduction, the historical observations revealed a prominent
420 modulation of the tidal range along the Amazon estuary, along the course of the high-
421 low flow annual cycle (Kosuth et al., 2009). Essentially, a tidal wave propagating
422 inside an estuary can be seen as a damped shallow-water gravity wave traveling
423 through a counter-current. In the Amazon estuary, just like in most high-discharge
424 estuaries, two key parameters vary jointly during the annual cycle that are bound to
425 condition the characteristics of the propagation of a tidal wave: the mean water level
426 and the residual flow velocity. During the high flow season, the water level is higher
427 and the flow velocity is larger than during the low flow season (Callède et al., 1996).
428 Through the shoaling effect, a higher water level will favor a lower tidal amplitude so
429 as to ensure wave energy flux conservation. Conversely, a higher water level will
430 induce a reduced bottom friction, which in turn decreases tidal dissipation. In the
431 particular case of an estuary bordered by vast floodplains such as the Amazon, a
432 higher water level is also prone to induce prominent flooding of extended intertidal
433 flats, which can act as a sink of tidal wave energy through bottom friction. As for the
434 river flow velocity, the theory predicts that it increases the damping of the incoming
435 tidal waves through frictional effects at the bottom, with a magnitude of the damping
436 force scaling roughly linearly with the magnitude of the residual river flow velocity
437 (e.g., Godin, 1999). These various processes altogether contribute to shape up the
438 seasonal modulation of the tide in the Amazon. Several studies have been based on
439 idealized and/or analytical models developed to infer the sensitivity of tidal
440 characteristics to estuarine hydrodynamical conditions (e.g., Du et al., 2018; Talke
441 and Jay, 2020, and the numerous references therein). However, it is challenging to
442 infer what will be the resulting impact of the seasonally-varying hydraulic regime on
443 the tide for an estuary with such a complex geometry as the Amazon. Indeed, the

idealized models typically assume regular cross-section geometry (Du et al., 2018) and/or linearized hydrodynamics (Talke and Jay, 2020). Our numerical model, as it explicitly accounts for all the processes mentioned above and their interactions, offers an unprecedented opportunity to investigate the seasonal modulation of the tidal characteristics.

4.1 Tidal influence along the estuary

The water level evolution at Óbidos, Almeirim, and Escola do Igarapé Grande stations are presented in Figure 3, along with the water level profile along the river and its tidal envelope computed separately for the high flow period (May 2018) and the low flow period (October 2018). The tidal envelope is here again defined as the syzygy amplitude, and a proxy of it was computed in the classical way from the sum of S2 and M2 amplitudes (Pugh and Woodworth, 2014), as these constituents are the main contributing components of the tide in our region.

While the seasonal pulse of the river flow induces annually a 6 m change in water level at Óbidos, this pulse decays downstream down to negligible values at the mouth (Figure 3). Conversely, the tidal amplitude amounts to 3 m at the mouth in Escola do Igarapé Grande, it decays upstream inside the estuary, with a tidal amplitude two orders of magnitude inferior in Óbidos. Hence the intermediate part of the estuary lies under the combined influence of both forcing factors. For instance, in Almeirim, located 397 km downstream of Óbidos in the middle reach of the estuary, the annual variation in water level due to the Amazon discharge is 4 m while the tidal range varies from 40 cm (May) to 90 cm (October) (Figure 3).

Figure 3b shows that the semi-diurnal tide is highly variable at seasonal timescales across the Amazon estuary. The reduction and increase of the Amazon River discharge cause an increase and reduction of the tidal amplitude, respectively. This variability implies that the extent of the tidal influence is itself highly variable along the seasonal cycle. It is seen that in high flow, the upstream limit of the tidal part of the estuary lies around 300 km from Óbidos; further upstream, the tidal signature virtually disappears. In contrast, in the low flow season, this limit is shifted towards upstream, up to Óbidos, where the open boundary of our model domain sits. Around 535 km from Óbidos, the range of the seasonal variability of the water level is

similar to the tidal range. Upstream of this limit, the water level variability is dominated by the annual hydrologic cycle, whereas downstream of it, it is dominated by the tide. Figure 4 shows that, at a given distance upstream of the mouth, the mean water level is quite alike among the various tributaries of the delta, so that it can be largely seen as primarily dependent on the distance from the mouth. It is seen that the mean slope of the water line is not constant, as it is steeper over the upstream part of the estuary. This reflects the complex, spatially variable geometry of the riverbed from upstream to downstream (Fricke et al., 2019; Fassoni-Andrade et al., 2021).

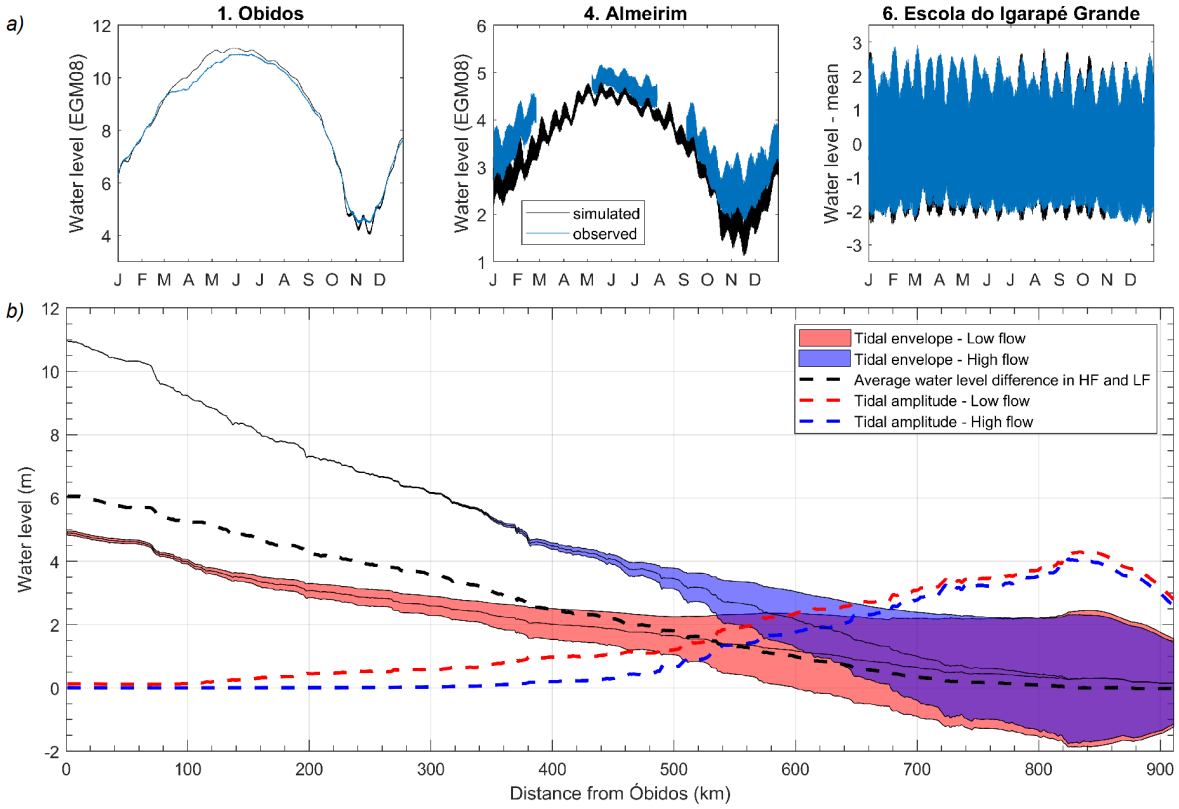

Figure 3. a) Evolution of the simulated and observed water level in Óbidos, Almeirim, and Escola Igarapé Grande over 2018; b) Simulated mean water level and tidal envelope along the Amazon River during May 2018 (high flow) and October 2018 (low flow).

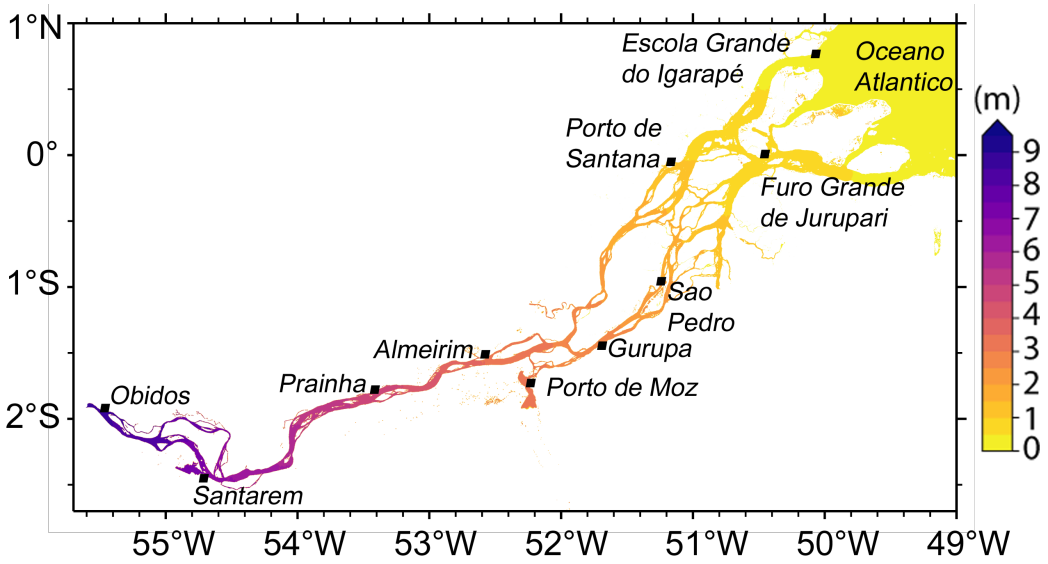

Figure 4. Simulated mean water level over 2018.

4.2 Tide amplitude

Figure 5 shows the seasonal evolution of M2 constituent and the tidal amplitude obtained along the river for 2018. The tidal amplitude in the reach between Óbidos and Porto de Santana (station 5) is prominently influenced by the Amazon River variability, with higher tidal amplitude during the low flow season (Oct/Nov) and conversely lower tidal amplitude during the high flow season (May/Jun). There does not appear to be any appreciable time lag between the variability of the tidal amplitude and the river discharge or river stage, which reveals the dominant role of three combined effects, among the various processes listed above: interaction between tide and river flow, interaction between tide and floodplains, and shoaling effect on the tidal waves. First, during the high flow season, over a given reach, the tidal wave propagates against a stronger counter-current, which induces a larger energy dissipation through bottom friction in the course of the propagation (Godin, 1999). Second, during the high flow season the river largely extends over the adjoining shallow floodplains, inducing additional sinks of energy of the tidal waves through bottom friction. Third, the linear shoaling effect may also contribute to reduced tidal amplitude when the water column is thicker. However, assessing the respective role of each of these three processes is beyond our scope.

The seasonal range of modulation of the tide is higher in the upstream reach. For example, considering the 20 cm isoline, the tidal amplitude gets shifted downstream by 290 km between November and May (Figure 5c). This variability reduces to the location where the Amazon River discharge no longer significantly influences the tidal amplitude (~700 km from Óbidos). This behavior implies that the frequent floods reported in Macapá (e.g., Mansur et al., 2016), the capital city of Amapá state located ~720 km from Óbidos nearby Porto de Santana (Figure 1) may not be related to the river floods, but rather to the tide and/or other oceanic influences. It is seen that the total tidal amplitude consistently presents a spatio-temporal pattern very similar to the sole M2 amplitude, M2 typically amounting to about 80% of the tidal range in the lower part of the Amazon. In the central part, the relative share of M2 decreases to about 60-70%. This is in line with the known dominance of M2 in the lower estuary, and its subsequent decay further upstream where M4 constituent picks up (Table A1; Gallo and Vinzon, 2005).

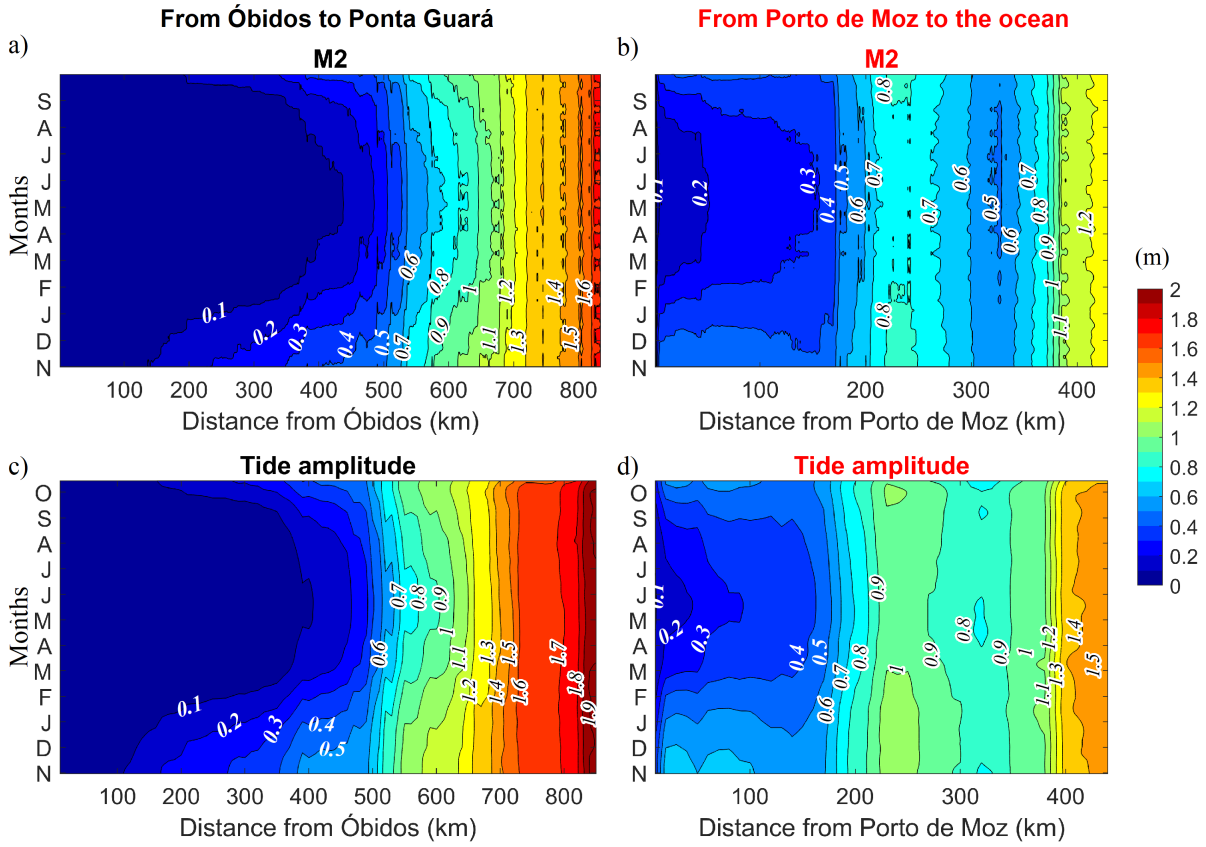

Figure 5. Tidal amplitude variability along the river in 2018. In (a) and (b), the amplitude of M2 (the dominant tidal constituent) is shown. In (c) and (d), the tidal amplitude is defined as the difference between daily maximum level and daily

minimum level (in a 25-hr moving window), subsequently low-pass-filtered with 28-day cutoff period to discard the spring-neap cycle that dos not form our focus. The left plots correspond to the reach between Óbidos and the ocean, and the right plots to the stretch between Porto de Moz and the ocean.

The amplitude of M2 monotonically decays in the Northern channel (Figure 5a and c). In contrast, in the Southern channel, a second section appears, between 220 km and 310 km from Porto de Moz, where the amplitude of M2 increases again (Figure 5b). This pattern is also seen in the total tidal amplitude (Figure 5d). This reach comprises the Breves Channel confluence, connecting the Amazon River to the Para-Tocantins estuary (Figure 1). Since we have no observations in this region, it is not possible to confirm the realism of this tidal amplitude pattern. In addition, we remind that we impose an outflowing boundary condition through the Breves Channel, amounting to 1% of the Amazon discharge injected at Óbidos at any time. The seasonal pattern of this boundary condition is the same as in Óbidos (minimum in October and maximum in May). In the absence of any temporal record of this throughflow (apart from the minimal data of Callède et al., 2010), the accuracy of this boundary condition is also questionable. In our model, however, this Breves Channel is subject to the tidal resonance of the semi-diurnal constituents, with an amplification of 25% of M2 amplitude, for instance, between the entrance and the head of the channel (not shown). This resonance of semi-diurnal constituents is consistent with the 30% amplification foreseen by the idealized model of Talke and Jay (2020), given the geometry of this channel. In turn, this resonance appears to induce leakage of tidal energy in the confluence of the Breves Channel and the Southern Channel of the Amazon, hereby inducing this secondary maximum located 220 km downstream of Porto de Moz in our model (Figure 5b and d). To confirm the realism of this feature, it would require assessing the water flow through the Breves Channel and the profile of tidal amplitude along its course.

4.3 Tidal wave celerity

The upstream propagation of the tidal wave along the estuary is expected to show a variable phase speed, depending on the seasonal variability of river level and

565 river flow velocity. In theory, a higher river level would induce a quicker phase speed
566 of the tidal wave in the absence of river flow. Nevertheless, a higher river level is
567 typically associated with a larger river flow velocity (Callède et al., 1996), which will
568 mechanically reduce the tidal wave speed. Kosuth et al. (2009) concluded that, over
569 the downstream half of the estuary, the observed change in tidal wave speed
570 (defined as the velocity of the tidal high water level across pairs of gauging stations)
571 increases from the high flow period to the low flow period.

572 We assessed the phase speed of the M2 wave between pairs of stations
573 (Table 2) from Óbidos to the ocean in both channels from our model simulation. Our
574 results agree with the findings of Kosuth et al. (2009) in the sense that the M2 wave
575 celerity increases in the low flow period (October) compared to the high flow period
576 (June). The largest increases are observed in the reach between Prainha and
577 Gurupá, with increases of 27% in the reach Prainha-Almeirim, and 33% between
578 Porto de Moz and Gurupá. On the other hand, the increase does not exceed 10% in
579 the downstream half of the estuary. The apparent negative velocity between
580 Camarão Tuba and Chaves is illustrated by the smaller phase in Camarão Tuba
581 relative to Chaves (see observed and simulated in Figure 2). As the amplitude of M2
582 tide increases between Chaves and Camarão Tuba, this suggests a resonant
583 process or the development of a standing wave in this stretch of the terminal delta
584 connected to the ocean through two separated channels (Figure 1).

585

586 Table 2. Time of propagation and celerity of M2 wave, and increase in wave celerity
587 (%) between low and high flow periods in river reaches. Some reaches upstream in
588 the high flow period were not filled due to the absence of tide

				Time of propagation (h)		Celerity (m/s)		Increase (%)
From Óbidos to the ocean	Downstream station	Upstream station	Reach length (km)	High flow	Low flow	High flow	Low flow	
	2.Santarém	1.Óbidos	115.83	-	2.85	-	11.28	-
	3.Prainha	2.Santarém	169.08	4.73	3.79	-	12.39	-
	4.Almeirim	3.Prainha	112.17	3.69	2.68	8.44	11.63	27.41
	5.Porto de Santana	4.Almeirim	275.26	6.59	5.68	11.60	13.47	13.90
	6.Escola Igarapé Grande	5.Porto de Santana	154.77	4.33	4.26	9.92	10.10	1.76

	7.Ponta Guará	6.Escola Igarapé Grande	65.00	1.38	1.32	13.05	13.69	4.67
	7.Ponta Guará	4.Almeirim	495.03	12.31	11.25	11.17	12.22	8.59
From Porto de Moz to the ocean	9.Gurupá	8.Porto de Moz	73.56	2.05	1.37	9.98	14.96	33.30
	10.São Pedro	9.Gurupá	84.07	1.97	1.89	11.87	12.34	3.81
	11.Furo Grande de Jurupari	10.São Pedro	134.27	4.13	3.88	9.02	9.60	6.00
	12.Camarão Tuba	11.Furo Grande de Jurupari	63.24	4.13	4.03	4.25	4.36	2.47
	13.Chaves	12.Camarão Tuba	49.93	-0.95	-0.98	-14.56	-14.18	-2.70
	14.Cabo Maguari	13.Chaves	130.00	3.65	3.67	9.88	9.84	-0.36
	14.Cabo Maguari	8.Porto de Moz	535.07	14.98	13.86	9.92	10.72	7.47

4.4 Water flow reversal

In the coastal ocean, a commonly known feature of the tide is the complete reversal of the tidal flow between the rising tide and the falling tide (e.g., Pugh and Woodworth, 2014). The picture is more complex in estuaries, as the tidal current is superimposed on (and interacts with) the background river flow. Close to the Amazon estuary mouth, where the river arms are typically broad and the semi-diurnal tide is powerful, the tidal influence remains prominent on the flow, with consistent reversals occurring twice daily throughout the seasonal cycle (Less et al., 2021). In contrast, in the upstream part of the estuary, it can be expected that the tidal velocities are overwhelmed by the background river velocity so that no reversal ever occurs (Callède et al., 1996). As Kosuth et al. (2009) reported from a limited set of cross-sectional ADCP surveys, the observed pattern of water flow along a tidal cycle is highly dependent on the location considered along the Amazon estuary: whereas a flow reversal is common in the downstream part of the estuary during the rising tide, it is not always so in its intermediate portion (typically in the region of the confluence at the beginning of the deltaic region, 500 km downstream of Óbidos), and it was never observed some 100 km further upstream, around Almeirim (station 4). There,

608 they reported that the river flow velocity decreases during the rising tide, but not
609 enough to get reversed. The location of the boundary between the two regimes
610 (always flow towards downstream vs. flow alternately towards upstream and towards
611 downstream during the tidal cycle) and its displacements along the seasonal cycle
612 are unknown due to the limited number of current-meter sections existing in the
613 observational records. The knowledge of this boundary bears some relevance, for
614 the understanding of the sediment dynamics in the estuary, for characterization of the
615 spatial dynamics of the ecosystems of the area (such as transports of fish larvae), for
616 the understanding of the biogeochemistry, or more generally of the chemical cycles
617 in the water body, and more basically for navigation-related issues.

618 We analyzed this regime boundary by computing the ratio between the daily
619 maximum along-channel velocity at ebb and at flood. Such a ratio means that
620 wherever negative values are seen, flow inversion occurs; conversely, positive
621 values mean that the flow is consistently downstream across the tidal cycle. The ratio
622 magnitude indicates the residual flow dominance over the tidal flow. Figure 6a and b
623 display the ratio, after applying a 28-day moving average, and Figure 6c shows the
624 portion of the estuary subject to at least one current reversal occurring over a 28-day
625 tidal cycle. It is seen that the location of this regime shift (seen as the null isocontour)
626 lies around 500 km downstream of Óbidos on average (Figure 6a), consistently with
627 the observations reported by Kosuth et al. (2009). However, this boundary gets
628 markedly displaced between the high flow season and the low flow season, with
629 extreme positions some 500 km and 670 km downstream of Óbidos (almost in Porto
630 de Santana – station 5) during the low flow season and the high flow season,
631 respectively. A similar spatio-temporal pattern of the boundary of the velocity regime
632 is seen in the southern channel, with a flow reversal boundary shifting from 100 km
633 downstream of Porto de Moz during the low-flow season to 250 km from Porto de
634 Moz during the high flow season (Figure 6b). These displacements result from the
635 combined effect of stronger residual flow velocity of the Amazon River and weaker
636 tidal current during the high flow season at any given location along the estuary. The
637 reach located in the Xingu River, upstream of the confluence of Xingu River and the
638 Amazon (~50 km in length, from Porto de Moz), also experiences an extended flow
639 inversion period from July to February (Figure 6b), probably related to the
640 consistently weak Xingu River discharge (Figure 1) combined with the relatively

strong tide arriving there from the Amazon. A couple of isolated red dots (viz. no flow reversal) are seen within the stretch of seasonally-occurring flow reversal in the Northern channel, around 575km from Óbidos. These are related to the localized pattern of velocity ratio seen at this location in Figure 6a, that remains positive there, even during the peak low flow season in November-December. This feature is related to the local change in the river geometry, where a reduced cross-section induces an increased residual flow velocity of the river. However, the velocity ratio reaches values very close to zero in the low flow season there, so that the large-scale pattern we pictured from upstream to downstream of the estuary remains valid.

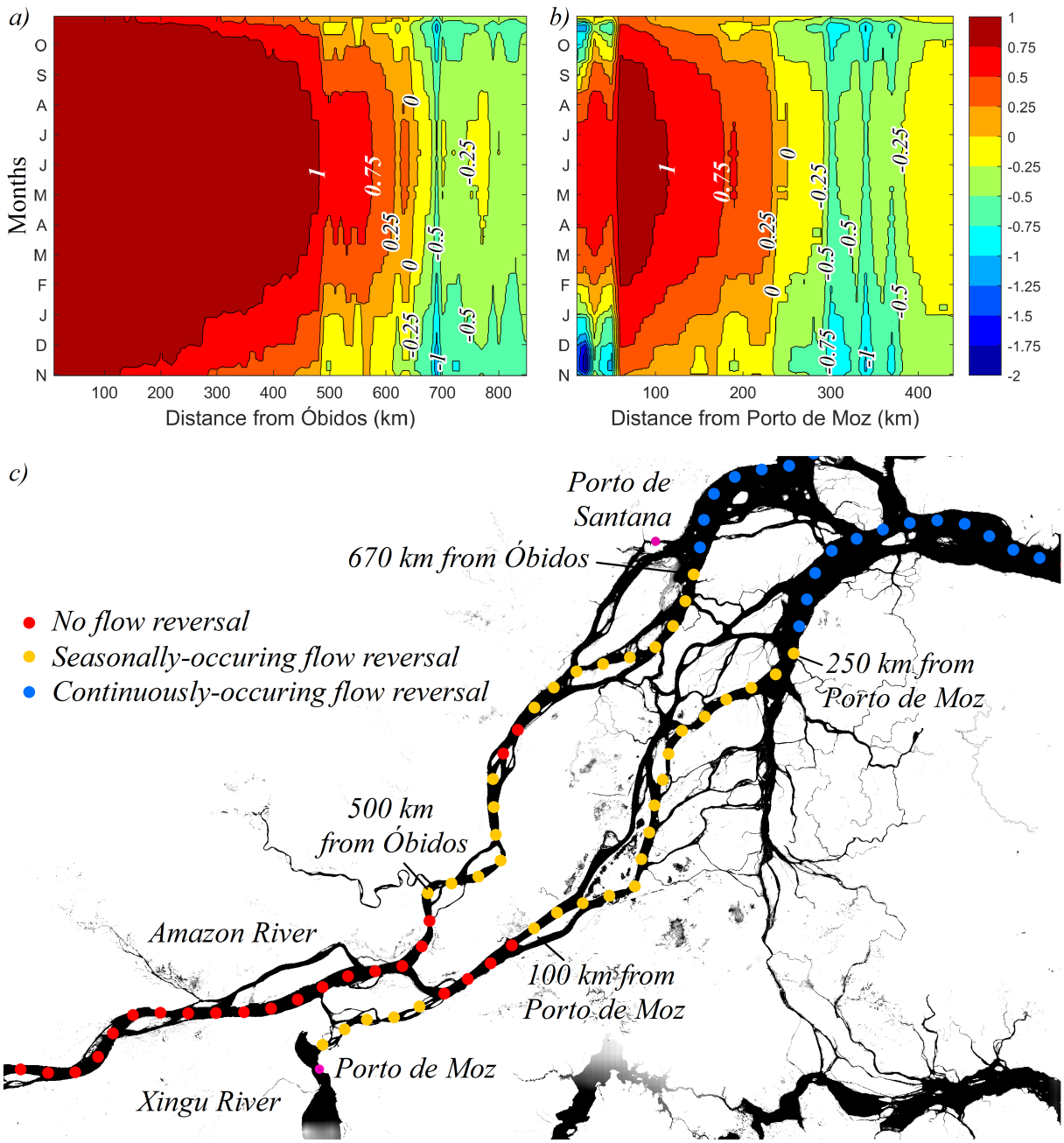

Figure 6. Space-time structure of the regime of the tidal flow reversal (ratio between the daily maximum velocity at ebb and flood) of the Amazon estuary for (a) the Northern channel and (b) the Southern channel. In yellow are the regions where the flow is consistently towards downstream, whereas in blue are the regions where the flow reverses towards upstream at least once during a 28-day tidal cycle. (c) Map of the tidal flow regimes of the Amazon estuary. The locations where the river flow reverses at least once over a 28-day tidal cycle are displayed in blue bullets (when this occurs year-round) and yellow bullets (when this happens in some seasons only). The locations where this reversal of the river flow never occurs are in red bullets.

5. Characteristics of the tide during extreme years

Beyond the seasonal timescale, it appears interesting to assess the impact of the interannual variability on the characteristics of the tide in the Amazon estuary, as the magnitude of the yearly freshwater discharge exhibited a marked interannual variability over the past decade, particularly in the 2014-2016 period.

Interannual variability of the tide due to non-astronomical factors has already been reported in other regions (e.g., Haigh et al., 2020, and references therein). For instance, Devlin et al. (2017) concluded that it could be significant indeed in several regions along the Pacific Ocean shoreline for instance. Jay et al. (2011) investigated the long-term changes of the tidal characteristics in the lower Columbia River (west coast of the United States), in response to the changes in river regime (among other factors). However, to the best of our knowledge, this issue has never been investigated in the Amazon estuary. We considered our model hindcast of both extreme floods and extreme drought periods that occurred between 2014 and 2016. These were compared with the year 2018, a year of roughly normal discharge conditions. The floods of June 2016 (discharge, Q=200 thousand $m^3.s^{-1}$) and June 2014 (Q=250 thousand $m^3.s^{-1}$) represent below and above average discharge respectively (with Q in 2018 peaking at 225 thousand $m^3.s^{-1}$) (Figure 7a). The low flow period of November 2014 (Q=113 thousand $m^3.s^{-1}$) and November 2015 (Q=81 thousand $m^3.s^{-1}$) represent above and below average discharge, respectively, the climatological low flow value amounting to 100 thousand $m^3.s^{-1}$ (Figure 7a). The tidal

amplitude variations along the river and the tidal range difference between the extreme years and the normal year (2018) are presented in Figure 7b-e.

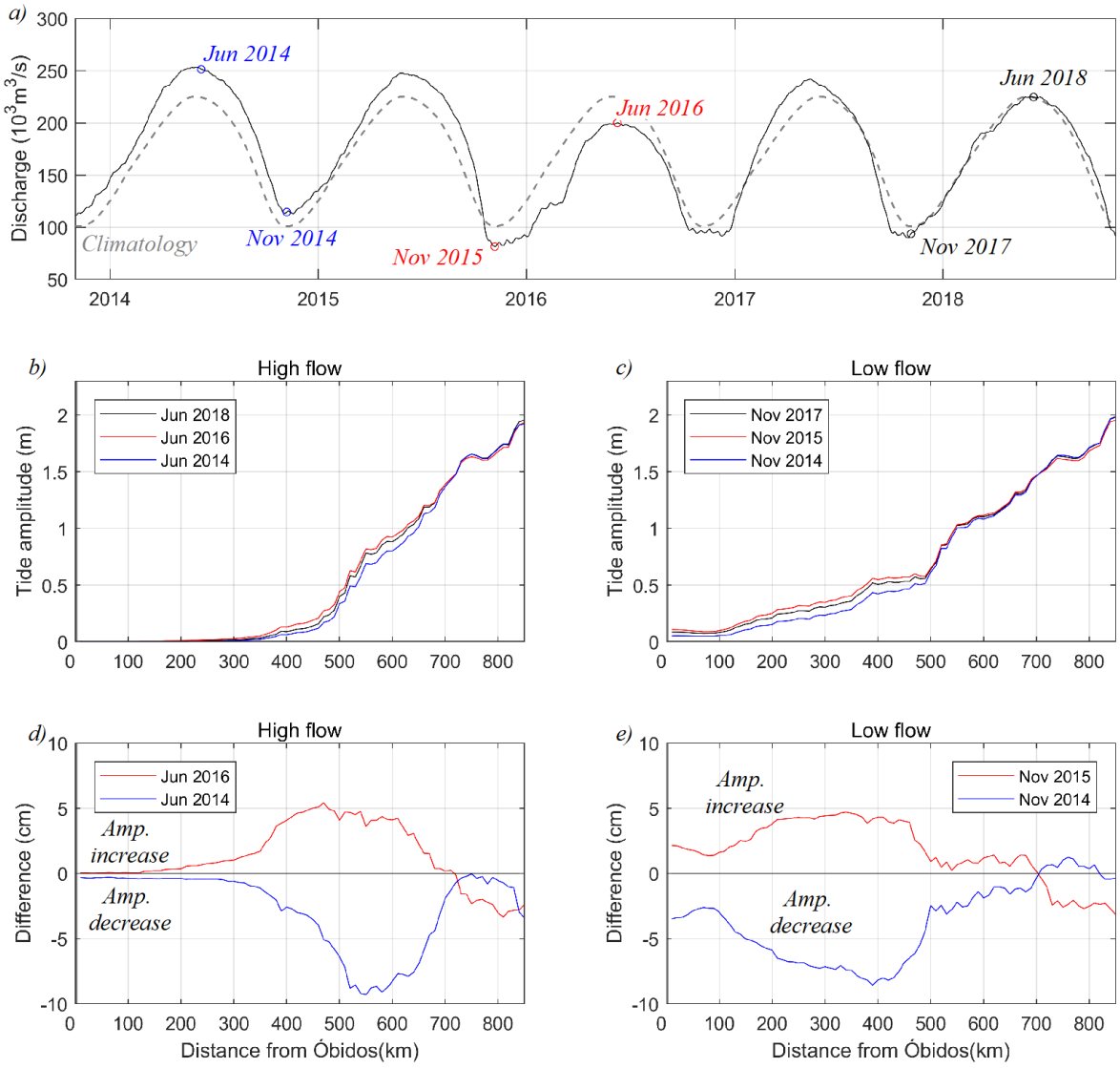

Figure 7. a) Amazon discharge climatology (1968-2020, dashes) and interannual evolution (solid) observed between 2014 and 2018; Profile of tidal amplitude along the river in high flow season (b) and low flow season (c); Tidal amplitude difference between the extreme years and the typical year (2018) in high flow season (d) and in the low flow season.

The interannual pattern of year-to-year modulation of the tidal amplitude is in line with the seasonal picture described in Section 4, with excess discharge yielding

lower tidal amplitude and vice-versa lower discharge associated with higher tidal amplitude, both in low and high flow seasons. However, the influence of interannual discharge anomaly on tidal amplitude strongly varies along the river course and among the periods considered. In the high flow period, above-average (2014) and below-average (2016) discharge affect the tidal amplitude mainly over the reach located between 200 km and 720 km from Óbidos, with variations of up to 8 cm in amplitude, in absolute values (Figure 7d). This maximum difference is seen between 500 km and 600 km and typically amounts to 10% of the tidal amplitude there. Further downstream, the anomalies reduce until ~720 km from Óbidos, where they virtually disappear. This implies that the tidal range in the downstream half of the terminal delta (typically downstream of Porto de Santana – Station 5) is primarily unaffected by the severe floods that occur interannually in the Amazon River. Above- and below-average floods do not appear to affect tidal range in the upstream-most reach, with tidal range variability being seen only 200 km downstream of Óbidos (between Monte Alegre and Santarém cities) and further downstream, regardless of flood magnitude (Figure 7d).

The anomalies of tidal amplitude in years with a lower (November 2015) and higher (November 2014) low flow period mimic the response during extreme floods, with excess low flow yielding negative tidal amplitude anomaly, and deficient low flow yielding positive tidal amplitude anomaly. The anomalous patterns extend over a longer reach than in the high flow period. The extent to which the Amazon River discharge influences the tidal range amounts to ~700 km, from Óbidos to Porto de Santana (station 5; Figure 7e). However, our model domain starts at Óbidos, where the tidal amplitude ranges from 5 cm (Nov/2014) to 10 cm (Nov/2015). This implies that the tidally-influenced river stretch extent may be even larger, extending to the region upstream of Óbidos. The anomaly of tidal amplitude along the river can reach 7 cm in the surroundings of Almeirim (station 4, ~400 km from Óbidos), amounting to 20% of the tidal range there. In this region, apart from the interaction between the tide and the anomalously low discharge, the river's connection with the extended shallow floodplains may also be significantly altered during extreme droughts and, in turn, may impact the tidal dynamics. However, the lack of tidal records in these floodplains precludes us from further investigating this issue. Downstream of this

region, the discharge has less influence on the tidal range (and the anomalies even reverse sign) downstream of Porto de Santana (~700 km from Óbidos).

6. Conclusion

This study investigated the seasonal and interannual variability of the tide along the Amazon River estuary through a novel, cross-scale, high resolution hydrodynamic numerical modeling platform duly validated against the available observations. Our findings show that the variability of the Amazon discharge has a significant influence on the magnitude and extent of the tidal propagation, on the tidal wave celerity, and the occurrence and magnitude of tidal flow reversal. This concerns the seasonal cycle as well as the year-to-year variability, both in the high flow season and in the low flow season.

The Amazon is the river with the largest discharge so that the monomodal flood pulse continuously affects the extent of tidal influence along the estuary. Our findings allow us to divide the estuary into the three following stretches: first, between Óbidos and 300 km downstream of Óbidos, a stretch where the water level is primarily influenced by the upstream watershed and only seasonally by the tide; second, between 300 km and 700 km from Óbidos (close by Prainha and Porto de Santana, respectively), a stretch where the water level is influenced by the river and by the tide throughout the year; third, a downstream stretch that is primarily influenced by the tide, between 700 km from Óbidos (around Porto de Santana) and the ocean.

The amplitude of M2 constituent decays from the vicinity of the mouths towards upstream, from a maximum reached about 100 km upstream of the oceanic outlets to a practically null value far upstream. The seasonal change follows the discharge pattern, with maximum values in October/November and minimum values in May/June.

At interannual timescales, the tidal amplitude varies significantly, by typically 10% during anomalous floods and up to 20-25% during anomalous droughts, primarily in the central reach of the estuary (from 300 km to 700 km upstream of the mouths). Nevertheless, the spatial extent of tidal anomalies along the Amazon River appears quite consistent among the various anomalous events of discharge we

759 considered. Indeed, regardless of the sign of the discharge anomaly, the influence on
760 the tidal range in June is limited to a reach of about 500 km length, starting 200 km
761 downstream of Óbidos and vanishing 700 km downstream of Óbidos. Similarly,
762 during the anomalous droughts (November), the imprint on the tidal range extends
763 from Óbidos to 700 km downstream of Óbidos, irrespective of the sign of the drought
764 anomaly.

765 The present description of the tidal characteristics of the Amazon may help to
766 understand the dynamics of the extreme events of water level and of the associated
767 spatio-temporal structure of the dryings and floodings, which have profound impacts
768 on the socio-economy of the riparian population (e.g., Mansur et al., 2016).
769 Furthermore, we believe our modeling study also contributes to paving the way for a
770 better understanding of the sediments dynamics as well as of the biogeochemical
771 cycles over the region.

772 As described in section 3, our modeling platform is not free of limitations. A re-
773 visit of the present conclusions once the various limitations can be alleviated will
774 certainly be timely.

775 A key issue in understanding the hydrodynamics of the Amazon estuary is the
776 lack of a dense-enough, high-quality, operational monitoring network of the water
777 level. The existing in situ monitoring stations used thoroughly in the present study are
778 few and the available records suffer from frequent data gaps and observational
779 issues, both on account of the enormity of the area and its difficult access.

780 Further analysis is needed to evaluate the estuary extent in the extreme low
781 flow periods, since our model domain is limited to the region from Óbidos to the
782 ocean. However, there are indications that the tide affects the water level in the
783 region upstream of Óbidos in such extreme drought periods, even if the tidal
784 amplitudes remain very small there (<4 cm). In this sense, a further upstream
785 extension of our model domain appears appropriate.

786 Finally, the Amazon estuary is probably currently experiencing its last epoch of
787 pristine hydrodynamical regime. Indeed the Amazon watershed faces anthropogenic
788 changes in its upstream parts that may impact its hydrological budget (Latrubesse et
789 al., 2017). Moreover, the Amazon basin is affected by climate variability, with 7 of the
790 latest 10 strongest floods since 1903 recorded in the past 13 years (Chevuturi et al.,

2022). The estuary is also subject to the ongoing sea level rise. Bearing in mind the very significant tidal modulation reported here at annual to interannual timescales, it is expected that the ongoing long-term changes of oceanic water level will also exert significant impacts on the tidal characteristics. Therefore, it will be essential to monitor and assess this long-term evolution and the associated water level extremes.

Acknowledgments

This research has been supported by Horizon 2020 (EOSC-SYNERGY project, grant number 857647). In addition, we are thankful to Marinha do Brasil, IBGE, ANA, CPRM and SO HYBAM-IRD for the provision of the tide gauge records. Valdenira Ferreira dos Santos (IEPA) provided the Ponta Guará tide gauge data. Furthermore, supercomputing facilities were provided by the HPC resources of IDRIS under the allocation 2021-A0090107298 granted by GENCI.

References

Allain, D.J., 2016. TUGOm Tidal Toolbox (ftp://ftp.legos.obs-mip.fr/pub/ecola/tools/ttb.pdf).

Andersen, O.B., Woodworth, P.L., Flather, R.A., 1995. Intercomparison of recent ocean tide models. J. Geophys. Res. Ocean. 100, 25261–25282. https://doi.org/10.1029/95JC02642

Armijos, E., Crave, A., Espinoza, J.C., Filizola, N., Espinoza-Villar, R., Ayes, I., Fonseca, P., Fraizy, P., Gutierrez, O., Vauchel, P., Camenen, B., Martiınez, J.M., Dos Santos, A., Santini, W., Cochonneau, G., Guyot, J.L., 2020. Rainfall control on amazon sediment flux: Synthesis from 20 years of monitoring. Environ. Res. Commun. 2. https://doi.org/10.1088/2515-7620/ab9003

Beardsley, R.C., Candela, J.L., Limeburner, R., Geyer, W.R., Lentz, S.J., Castro, B.M., Cacchione, D.A., Carneiro, N., 1995. The M2 tide on the Amazon Shelf. J. Geophys. Res. C Ocean. 100, 2283–2319. https://doi.org/10.1029/94JC01688

Birkett, C.M., Mertes, L.A.K., Dunne, T., Costa, M.H., Jasinski, M.J., 2002. Surface water dynamics in the Amazon Basin: Application of satellite radar altimetry. J. Geophys. Res. D Atmos. 107. https://doi.org/10.1029/2001JD000609

Bunya, S., Dietrich, J.C., Westerink, J.J., Ebersole, B.A., Smith, J.M., Atkinson, J.H., Jensen, R., Resio, D.T., Luettich, R.A., Dawson, C., Cardone, V.J., Cox, A.T., Powell, M.D., Westerink, H.J., Roberts, H.J., 2010. A High-Resolution Coupled Riverine Flow, Tide, Wind, Wind Wave, and Storm Surge Model for Southern Louisiana and Mississippi. Part I: Model Development and Validation. Mon. Weather Rev. 138, 345–377. https://doi.org/10.1175/2009MWR2906.1

Cai, H., Savenije, H.H.G., Toffolon, M., 2014. Linking the river to the estuary:

influence of river discharge on tidal damping. Hydrol. Earth Syst. Sci. 18, 287–304. https://doi.org/10.5194/hess-18-287-2014

Callède, J., Cochonneau, G., Alves, F.V., Guyot, J.-L., Guimarães, V.S., De Oliveira, E., 2010. The River Amazon water contribution to the Atlantic Ocean. Rev. des Sci. l'eau 23, 247–273.

Callède, J., Guyot, J., Guimarães, V.S., Oliveira, E. de, Naziano, F., 1996. As descargas do rio Amazonas em Óbidos. Report DNAEE-CGRH/CNPq/ORSTOM.

Carrère, L., Lyard, F.H., Cancet, M., Guillot, A., Picot, N., 2016. Finite Element Solution FES2014, a new tidal model – Validation results and perspectives for improvements, in: ESA Living Planet Conference. Prague.

Chevuturi, A., Klingaman, N.P., Rudorff, C.M., Coelho, C.A.S., Schöngart, J., 2022. Forecasting annual maximum water level for the Negro River at Manaus. Clim. Resil. Sustain. 1, 1–17. https://doi.org/10.1002/cli2.18

Clarke, A.J., Battisti, D.S., 1981. The effect of continental shelves on tides. Deep Sea Res. Part A. Oceanogr. Res. Pap. 28, 665–682. https://doi.org/https://doi.org/10.1016/0198-0149(81)90128-X

Devlin, A.T., Jay, D.A., Zaron, E.D., Talke, S.A., Pan, J., Lin, H., 2017. Tidal Variability Related to Sea Level Variability in the Pacific Ocean. J. Geophys. Res. Ocean. 122, 8445–8463. https://doi.org/10.1002/2017JC013165

Du, J., Shen, J., Zhang, Y.J., Ye, F., Liu, Z., Wang, Z., Wang, Y.P., Yu, X., Sisson, M., Wang, H. V, 2018. Tidal Response to Sea-Level Rise in Different Types of Estuaries: The Importance of Length, Bathymetry, and Geometry. Geophys. Res. Lett. 45, 227–235. https://doi.org/10.1002/2017GL075963

Durand, F., Testut, L., Jouanno, J., Fassoni-Andrade, A.C., 2022. Role of the amazon outflow on the barotropic tide on the amazonian shelf. Cont. Shelf Res. 238, 104695. https://doi.org/10.1016/j.csr.2022.104695

Elahi, M.W.E., Jalón-Rojas, I., Wang, X.H., Ritchie, E.A., 2020. Influence of Seasonal River Discharge on Tidal Propagation in the Ganges-Brahmaputra-Meghna Delta, Bangladesh. J. Geophys. Res. Ocean. 125, e2020JC016417. https://doi.org/10.1029/2020JC016417

Eslami, S., Hoekstra, P., Kernkamp, H., Nguyen Trung, N., Do Duc, D., Tran Quang, T., Februarianto, M., Van Dam, A., van der Vegt, M., 2019. Flow Division Dynamics in the Mekong Delta: Application of a 1D-2D Coupled Model. Water 11. https://doi.org/10.3390/w11040837

Fassoni-Andrade, A.C., Durand, F., Moreira, D., Azevedo, A., Santos, V., Funi, C., Laraque, A., 2021. Comprehensive bathymetry and intertidal topography of the Amazon estuary. Earth Syst. Sci. Data 13, 2275–2291. https://doi.org/10.5194/essd-13-2275-2021

Fontes, R.F.C., Castro, B.M., Beardsley, R.C., 2008. Numerical study of circulation on the inner Amazon Shelf. Ocean Dyn. 58, 187–198. https://doi.org/10.1007/s10236-008-0139-4

Fortunato, A., Oliveira, A., 2005. Influence of Intertidal Flats on Tidal Asymmetry. J. Coast. Res. 21(5), 1062–1067.

Fricke, A.T., Nittrouer, C.A., Ogston, A.S., Nowacki, D.J., Asp, N.E., Souza Filho,

P.W.M., 2019. Morphology and dynamics of the intertidal floodplain along the Amazon tidal river. Earth Surf. Process. Landforms 44, 204–218. https://doi.org/10.1002/esp.4545

Gabioux, M., Vinzon, S.B., Paiva, A.M., 2005. Tidal propagation over fluid mud layers on the Amazon shelf. Cont. Shelf Res. 25, 113–125. https://doi.org/10.1016/j.csr.2004.09.001

Gallo, M.N., Vinzon, S.B., 2005. Generation of overtides and compound tides in Amazon estuary. Ocean Dyn. 55, 441–448. https://doi.org/10.1007/s10236-005-0003-8

Geyer, W.R., Kineke, G.C., 1995. Observations of currents and water properties in the Amazon frontal zone. J. Geophys. Res. 100, 2321–2339. https://doi.org/10.1029/94JC02657

Godin, G., 1999. The Propagation of Tides up Rivers With Special Considerations on the Upper Saint Lawrence River. Estuar. Coast. Shelf Sci. 48, 307–324. https://doi.org/10.1006/ecss.1998.0422

Guo, L., van der Wegen, M., Jay, D.A., Matte, P., Wang, Z.B., Roelvink, D., He, Q., 2015. River-tide dynamics: Exploration of nonstationary and nonlinear tidal behavior in the Yangtze River estuary. J. Geophys. Res. Ocean. 120, 3499–3521. https://doi.org/10.1002/2014JC010491

Haigh, I.D., Pickering, M.D., Green, J.A.M., Arbic, B.K., Arns, A., Dangendorf, S., Hill, D.F., Horsburgh, K., Howard, T., Idier, D., Jay, D.A., Jänicke, L., Lee, S.B., Müller, M., Schindelegger, M., Talke, S.A., Wilmes, S.B., Woodworth, P.L., 2020. The Tides They Are A-Changin': A Comprehensive Review of Past and Future Nonastronomical Changes in Tides, Their Driving Mechanisms, and Future Implications. Rev. Geophys. 58. https://doi.org/10.1029/2018RG000636

Helaire, L.T., Talke, S.A., Jay, D.A., Mahedy, D., 2019. Historical Changes in Lower Columbia River and Estuary Floods: A Numerical Study. J. Geophys. Res. Ocean. 124, 7926–7946. https://doi.org/10.1029/2019JC015055

Huang, W., Ye, F., Zhang, Y.J., Park, K., Du, J., Moghimi, S., Myers, E., Pe'eri, S., Calzada, J.R., Yu, H.C., Nunez, K., Liu, Z., 2021. Compounding factors for extreme flooding around Galveston Bay during Hurricane Harvey. Ocean Model. 158, 101735. https://doi.org/10.1016/j.ocemod.2020.101735

Jay, D.A., Leffler, K., Degens, S., 2011. Long-Term Evolution of Columbia River Tides. J. Waterw. Port, Coastal, Ocean Eng. 137, 182–191. https://doi.org/10.1061/(asce)ww.1943-5460.0000082

Junk, W.J., Piedade, M.T.F., Schöngart, J., Wittmann, F., 2012. A classification of major natural habitats of Amazonian white-water river floodplains (várzeas). Wetl. Ecol. Manag. 20, 461–475. https://doi.org/10.1007/s11273-012-9268-0

Khan, M.J.U., 2021. Dynamique des inondations dans le continuum rivières-estuaires-océan littoral du delta du Bengale : synergie modélisation hydrodynamique - télédétection spatiale.

Khan, M.J.U., Durand, F., Testut, L., Krien, Y., Islam, A.K.M.S., 2020. Sea level rise inducing tidal modulation along the coasts of Bengal delta. Cont. Shelf Res. 211, 104289. https://doi.org/10.1016/j.csr.2020.104289

Kineke, G.C., Sternberg, R.W., Trowbridge, J.H., Geyer, W.R., 1996. Fluid-mud

processes on the Amazon continental shelf. Cont. Shelf Res. 16, 667–696. https://doi.org/10.1016/0278-4343(95)00050-X

Kosuth, P., Callede, J., Laraque, A., Filizola, N., Guyot, J.L., Seyler, P., Fritsch, J.M., Guimarães, V., 2009. Sea-tide effects on flows in the lower reaches of the Amazon River. Hydrol. Process. 23, 3141–3150. https://doi.org/10.1002/hyp.7387

Krien, Y., Mayet, C., Testut, L., Durand, F., Tazkia, A.R., Islam, A.K.M.S., Gopalakrishna, V. V., Becker, M., Calmant, S., Shum, C.K., Khan, Z.H., Papa, F., Ballu, V., 2016. Improved Bathymetric Dataset and Tidal Model for the Northern Bay of Bengal. Mar. Geod. 39, 422–438. https://doi.org/10.1080/01490419.2016.1227405

Latrubesse, E.M., Arima, E.Y., Dunne, T., Park, E., Baker, V.R., D'Horta, F.M., Wight, C., Wittmann, F., Zuanon, J., Baker, P.A., Ribas, C.C., Norgaard, R.B., Filizola, N., Ansar, A., Flyvbjerg, B., Stevaux, J.C., 2017. Damming the rivers of the Amazon basin. Nature. https://doi.org/10.1038/nature22333

Le Bars, Y., Lyard, F., Jeandel, C., Dardengo, L., 2010. The AMANDES tidal model for the Amazon estuary and shelf. Ocean Model. 31, 132–149. https://doi.org/10.1016/j.ocemod.2009.11.001

Less, D.F.S., Ward, N.D., Richey, J.E., Da Cunha, A.C., 2021. Seasonal and Daily Variation of Hydrodynamic Conditions in the Amazon River Mouth: Influence of Discharge and Tide on Flow Velocity. J. Coast. Res. 37, 1181–1192. https://doi.org/10.2112/JCOASTRES-D-21-00010.1

Losada, M.A., D\'\iez-Minguito, M., Reyes-Merlo, M.Á., 2017. Tidal-fluvial interaction in the Guadalquivir River Estuary: Spatial and frequency-dependent response of currents and water levels. J. Geophys. Res. Ocean. 122, 847–865. https://doi.org/10.1002/2016jc011984

Mansur, A. V., Brondízio, E.S., Roy, S., Hetrick, S., Vogt, N.D., Newton, A., 2016. An assessment of urban vulnerability in the Amazon Delta and Estuary: a multi-criterion index of flood exposure, socio-economic conditions and infrastructure. Sustain. Sci. 11, 625–643. https://doi.org/10.1007/s11625-016-0355-7

Matte, P., Secretan, Y., Morin, J., 2014. Temporal and spatial variability of tida-fluvial dynamics in the St. Lawrence fluvial estuary: An application of nonstationary tidal harmonic analysis. J. Geophys. Res. 119, 5724–5744.

Melack, J.M., Amaral, J.H.F., Kasper, D., Barbosa, P.M., Forsberg, B.R., 2021. Limnological perspectives on conservation of aquatic ecosystems in the Amazon basin. Aquat. Conserv. Mar. Freshw. Ecosyst. 30. https://doi.org/10.1002/aqc.3556

Molinas, E., Carneiro, J.C., Vinzon, S., 2020. Internal tides as a major process in Amazon continental shelf fine sediment transport. Mar. Geol. 430. https://doi.org/10.1016/j.margeo.2020.106360

Molinas, E., Vinzon, S.B., de Paula Xavier Vilela, C., Gallo, M.N., 2014. Structure and position of the bottom salinity front in the Amazon Estuary. Ocean Dyn. 64, 1583–1599. https://doi.org/10.1007/s10236-014-0763-0

Nikiema, O., Devenon, J.L., Baklouti, M., 2007. Numerical modeling of the Amazon River plume. Cont. Shelf Res. 27, 873–899.

https://doi.org/10.1016/j.csr.2006.12.004

Nittrouer, C., DeMaster, D., Kuehl, S., Figueiredo, A., Sternberg, R., Faria, L.E.C., Silveira, O., Allison, M., Kineke, G., Ogston, A., Souza Filho, P., Asp, N., Nowacki, D., Fricke, A., 2021. Amazon Sediment Transport and Accumulation Along the Continuum of Mixed Fluvial and Marine Processes. Ann. Rev. Mar. Sci. 13, 1–36. https://doi.org/10.1146/annurev-marine-010816-060457

Potapov, P., Li, X., Hernandez-Serna, A., Tyukavina, A., Hansen, M.C., Kommareddy, A., Pickens, A., Turubanova, S., Tang, H., Silva, C.E., Armston, J., Dubayah, R., Blair, J.B., Hofton, M., 2021. Mapping global forest canopy height through integration of GEDI and Landsat data. Remote Sens. Environ. 253, 112165. https://doi.org/10.1016/j.rse.2020.112165

Pugh, D., Woodworth, P., 2014. Sea-Level Science: Understanding Tides, Surges, Tsunamis and Mean Sea-Level Changes, Oceanography. https://doi.org/10.5670/oceanog.2015.24

Ruault, V., Jouanno, J., Durand, F., Chanut, J., Benshila, R., 2020. Role of the Tide on the Structure of the Amazon Plume: A Numerical Modeling Approach. J. Geophys. Res. Ocean. 125, 1–17. https://doi.org/10.1029/2019jc015495

Sawakuchi, H.O., Neu, V., Ward, N.D., Barros, M. de L.C., Valerio, A.M., Gagne-Maynard, W., Cunha, A.C., Less, D.F.S., Diniz, J.E.M., Brito, D.C., Krusche, A. V, Richey, J.E., 2017. Carbon Dioxide Emissions along the Lower Amazon River. Front. Mar. Sci. 4, 76. https://doi.org/10.3389/fmars.2017.00076

Talke, S.A., Jay, D.A., 2020. Changing Tides: The Role of Natural and Anthropogenic Factors. Ann. Rev. Mar. Sci. 12, 121–151. https://doi.org/10.1146/annurev-marine-010419-010727

Testut, L., Unnikrishnan, A.S., 2016. Improving Modeling of Tides on the Continental Shelf off the West Coast of India. J. Coast. Res. 32, 105–115. https://doi.org/10.2112/JCOASTRES-D-14-00019.1

Yamazaki, D., Ikeshima, D., Tawatari, R., Yamaguchi, T., O'Loughlin, F., Neal, J.C., Sampson, C.C., Kanae, S., Bates, P.D., 2017. A high-accuracy map of global terrain elevations. Geophys. Res. Lett. 44, 5844–5853. https://doi.org/10.1002/2017GL072874

Zhang, Y.J., Ye, F., Stanev, E. V., Grashorn, S., 2016. Seamless cross-scale modeling with SCHISM. Ocean Model. 102, 64–81. https://doi.org/10.1016/j.ocemod.2016.05.002

Appendix

Table A.1. Amplitudes of the dominant constituents modeled in high and low flow

		Amplitude (cm)									
		Mm		Msf		M2		S2		M4	
		sim	obs	sim	obs	sim	obs	sim	obs	sim	obs
High flow	Óbidos	6.27	10.54	1.93	2.20	0.20	0.15	0.12	0.30	0.02	0.08
	Santarém	5.68	8.85	3.10	0.47	0.07	0.23	0.01	0.14	0.01	0.04
	Prainha	5.44	2.99	5.01	4.24	0.95	5.68	0.27	1.10	0.16	0.98

	Almeirim	7.54	5.43	9.11	4.47	7.60	16.96	2.11	2.88	1.74	3.94
	Porto de Santana	14.14	4.96	18.49	10.00	100.00	117.45	23.86	19.53	23.51	23.92
	Escola Igarapé Grande	6.28	12.07	8.58	13.05	165.24	170.60	41.43	35.11	19.33	20.28
	Ponta Guará	4.22	3.23	6.14	-	124.52	153.37	31.39	39.84	22.94	25.86
	Porto de Moz	8.52	10.60	11.14	10.07	10.20	4.04	2.84	0.62	2.67	1.46
	Gurupá	10.56	7.69	13.09	11.12	21.94	45.04	6.17	7.89	4.37	8.00
	São Pedro	9.74	12.53	12.85	18.07	22.16	62.76	5.75	9.03	4.48	11.44
	Furo Grande de Jurupari	12.64	10.36	16.47	-	59.26	90.92	16.05	29.54	17.20	19.26
	Camarão Tuba	8.06	9.55	10.03	-	114.11	152.12	34.11	40.94	27.17	27.79
	Chaves	10.91	8.29	13.93	-	64.24	116.98	20.45	20.65	29.64	30.29
	Cabo Maguari	5.20	23.99	6.02	-	147.25	131.40	40.78	37.82	24.56	22.15
Low flow	**Óbidos**	72.76	64.98	9.98	16.70	3.97	3.14	1.90	1.38	0.88	0.59
	Santarém	59.64	52.75	10.43	9.77	6.15	3.89	0.87	1.34	1.53	1.44
	Prainha	45.06	14.66	15.78	9.34	18.38	12.96	6.54	4.08	4.33	3.04
	Almeirim	34.18	20.54	19.42	6.40	34.09	37.06	10.88	9.51	9.45	10.65
	Porto de Santana	15.70	12.06	17.53	14.48	115.51	108.05	30.83	26.77	22.26	17.18
	Escola Igarapé Grande	5.37	3.56	8.91	10.04	175.01	169.60	50.85	38.16	20.07	14.81
	Ponta Guará	3.55	3.23	6.11	-	133.63	153.37	39.23	39.84	24.02	25.86
	Porto de Moz	30.41	11.72	19.34	11.54	39.73	10.09	12.10	2.67	12.66	4.67
	Gurupá	27.14	6.26	21.46	15.98	43.98	58.48	13.14	13.51	8.95	9.55
	São Pedro	31.64	12.53	12.88	18.07	42.94	62.76	14.06	9.03	8.86	11.44
	Furo Grande de Jurupari	12.48	10.36	16.33	-	66.06	90.92	21.31	29.54	15.44	19.26
	Camarão Tuba	7.12	9.55	11.22	-	120.69	152.12	43.36	40.94	25.42	27.79
	Chaves	10.24	8.29	14.78	-	70.85	116.98	26.87	20.65	27.59	30.29
	Cabo Maguari	3.91	23.99	8.34	-	154.81	131.40	51.13	37.82	21.97	22.15

1000

1001 Table A.2. Phases of the dominant constituents modeled in high and low **flow**

		Phase									
		Mm		**Msf**		**M2**		**S2**		**M4**	
		sim	**obs**	**sim**	**obs**	**sim**	**obs**	**sim**	**obs**	**sim**	**obs**
High flow	**Óbidos**	464.33	430.43	549.34	656.86	580.43	540.92	603.89	595.05	611.47	542.02
	Santarém	483.50	440.27	517.39	590.90	667.63	597.02	683.04	633.62	542.72	630.73
	Prainha	451.92	438.77	466.74	459.53	530.40	478.43	540.15	492.87	552.42	463.44
	Almeirim	415.26	374.53	433.89	475.62	423.37	403.84	433.39	423.29	379.69	713.99
	Porto de Santana	25.08	41.99	39.34	20.43	232.21	210.59	248.26	232.08	14.52	348.83

	Escola Igarapé Grande	6.48	21.86	39.60	48.35	106.55	93.57	120.51	116.73	111.52	111.85
	Ponta Guará	10.76	149.31	41.88	-	66.43	43.71	76.86	61.83	343.80	309.79
	Porto de Moz	408.74	407.73	431.03	438.92	411.41	389.33	418.38	406.64	361.10	686.70
	Gurupá	38.15	34.35	55.72	51.15	352.02	323.98	0.71	334.82	260.80	182.43
	São Pedro	24.75	43.00	44.79	31.36	294.98	278.13	306.06	301.83	111.718	87.99
	Furo Grande de Jurupari	19.05	14.70	37.03	-	175.16	165.68	183.08	192.40	231.40	265.40
	Camarão Tuba	6.73	26.21	34.36	-	55.38	74.97	73.10	79.88	83.87	80.95
	Chaves	13.60	332.59	35.71	-	83.00	93.62	98.98	136.51	137.96	121.88
	Cabo Maguari	-7.06	-10.45	-336.57	-	-22.96	0.64	-7.58	-341.55	-108.46	-60.11
Low flow	**Óbidos**	431.93	437.80	703.13	644.30	659.84	615.04	414.62	434.74	529.78	467.19
	Santarém	429.78	436.84	376.65	654.62	577.15	551.18	540.24	492.31	672.56	636.06
	Prainha	425.76	550.70	390.41	489.44	467.26	446.53	483.77	472.80	478.95	434.13
	Almeirim	421.23	416.14	391.18	360.64	389.56	378.66	411.48	406.62	708.28	700.97
	Porto de Santana	49.79	36.72	21.66	40.68	224.98	197.42	248.59	224.04	354.04	329.99
	Escola Igarapé Grande	42.35	7.06	6.05	29.90	101.52	88.96	122.65	113.69	105.31	108.90
	Ponta Guará	42.97	149.31	357.01	-	63.27	43.71	78.61	61.83	346.80	309.79
	Porto de Moz	420.62	401.97	393.25	408.69	376.20	368.52	394.86	380.46	684.98	670.68
	Gurupá	56.27	47.00	29.26	45.05	336.59	319.90	353.50	347.78	237.20	185.50
	São Pedro	41.3066	43.00	41.7019	31.36	281.722	278.13	298.02	301.83	83.4821	87.99
	Furo Grande de Jurupari	44.83	14.70	19.48	-	169.09	165.68	184.10	192.40	223.19	265.40
	Camarão Tuba	38.92	26.21	11.58	-	52.27	74.97	77.82	79.88	78.37	80.95
	Chaves	41.62	332.59	16.44	-	80.64	93.62	104.70	136.51	129.64	121.88
	Cabo Maguari	-320.36	-10.45	-352.39	-	-25.71	0.64	-3.85	-341.55	-112.50	-60.11

Table A.3. Complex error of the modeled tide at each station in high and low flow season (in cm)

Station	**High flow**	**Low flow**
Óbidos	4.52	7.72
Santarém	4.32	7.31
Prainha	4.20	39.24
Almeirim	8.18	11.22
Porto de Santana	33.28	39.80
Escola Igarapé Grande	27.89	29.14
Ponta Guará	45.90	39.83
Porto de Moz	5.30	26.75
Gurupá	20.68	21.62

São Pedro	23.13	16.47
Furo Grande de Jurupari	27.09	21.55
Camarão Tuba	42.03	43.91
Chaves	40.83	38.03
Cabo Maguari	47.61	55.19

1005